



Photoacoustic tomography reconstruction using lag-based delay multiply and sum with a coherence factor improves in vivo ovarian cancer diagnosis

GUANG YANG,¹  **EGHBAL AMIDI,¹**  **AND QUING ZHU^{1,2,*}** 

¹*Department of Biomedical Engineering, Washington University in St. Louis, St. Louis, MO 63130, USA*

²*Department of Radiology, Washington University School of Medicine, St. Louis, MO 63110, USA*

**zhu.q@wustl.edu*

Abstract: Ovarian cancer is the fifth most common cause of death due to cancer, and it is the deadliest of all gynecological cancers. Diagnosing ovarian cancer via conventional photoacoustic delay-and-sum beamforming (DAS) presents several challenges, such as poor image resolution and low lesion to background tissue contrast. To address these concerns, we propose an improved beamformer named lag-based delay multiply and sum combined with coherence factor (DMAS-LAG-CF). Simulations and phantom experiments demonstrate that compared with the conventional DAS, the proposed algorithm can provide 1.39 times better resolution and 10.77 dB higher contrast. For patient data, similar performance on contrast ratios has been observed. However, since the diagnostic accuracy between cancer and benign/normal groups is a significant measure, we have extracted photoacoustic histogram features of mean, kurtosis and skewness. DMAS-LAG-CF can improve cancer diagnosis with an AUC of 0.91 for distinguishing malignant vs. benign ovarian lesions when mean and skewness are used as features.

© 2021 Optical Society of America under the terms of the [OSA Open Access Publishing Agreement](#)

1. Introduction

Photoacoustic imaging (PAI), also known as optoacoustic imaging (OA), is an emerging biomedical imaging modality that uses the resolution of ultrasound imaging and the contrast of optical imaging to provide structural and functional information [1–2]. PAI has demonstrated its potential for image-based diagnosis in oncology (e.g., breast [3–4], thyroid [5–6], cervical [7], colorectal [8–9], ovarian [10–11], and prostate cancers [12–13]), peripheral vascular diseases (PVDs) [14], joint inflammations [15–17], and skin diseases [18–20].

Ranking fifth among fatal cancers affecting women, ovarian cancer accounts for more deaths than any other cancer of the female reproductive system. According to the American Cancer Society, about 21,750 women received a new diagnosis of ovarian cancer and about 13,940 women died from ovarian cancer in 2020 [21]. Due to the lack of early screening and diagnostic techniques, many women are diagnosed with ovarian cancer when it is already at stages III or IV, where the mortality rates are high (70 to 75%) [22]. Conventional screening tests, including pelvic examination [23,24], transvaginal ultrasound (TVUS) [25,26], and blood testing for cancer antigen 125 (CA-125) [26,27], lack sufficient specificity for early ovarian cancer diagnosis [27]. Imaging modalities such as computed tomography (CT), positron emission tomography (PET), and magnetic resonance imaging (MRI) have been used for surgical guidance. However, all of these modalities have limitations in detecting small lesions. In previous work, to address this limitation, we developed a co-registered photoacoustic and TVUS technique to improve ovarian cancer diagnosis [10,11].

Currently, clinical applications of photoacoustic (PA) or ultrasound (US) imaging most commonly use the delay and sum (DAS) beamforming algorithm. This algorithm simply sums the properly delayed and weighted PA/US signal from each channel according to the distances

between the focal points and the detectors. However, it has the drawbacks of low resolution and high side lobes, resulting in poor reconstructed image quality. Lim et al. first introduced the delay-multiply-and-sum (DMAS) image reconstruction algorithm for confocal microwave imaging used for breast cancer detection [28]. Subsequently, Matrone et al. proposed an improved version of DMAS to overcome the limitations of DAS in US imaging [29]. Because DMAS improves the coherence of detected channel data, it provides enhanced image quality, with narrower main lobes, and lower side lobes than DAS. These advantages have led several researchers to adopt DMAS in PA imaging and to propose new approaches combining DMAS with other methods. Park et al. combined DMAS with synthetic aperture focusing and applied it to PA microscopy [30]. Alshaya et al. applied DMAS to PA imaging, employing a linear array transducer and introducing a subgroup DMAS method to improve the SNR and processing speed [31]. Matrone et al. combined filtered DMAS (F-DMAS) with multi-line transmission to achieve high frame-rate and high resolution [32]. Mozaffarzadeh et al. combined the minimum variance (MV) beamforming algorithm with DMAS [33]. The MV adaptive beamformer [34] can dynamically calculate the signal weights of the received signals instead of using a fixed apodization function. However, it is very computationally demanding.

While all the above approaches are based on the single-stage DMAS method, Mozaffarzadeh et al. [35] proposed a double-stage DMAS (DS-DMAS) beamforming algorithm. They literally divided the process of beamforming into two stages. First, the signals are processed by DMAS, that is, the right side of the DMAS equation is expanded to the summations of the separate terms, and these summations are treated as several new synthesized signals. Second, the new synthesized signals are processed by the F-DMAS beamformer again to generate the final output. Same as DMAS, DS-DMAS further improves the image resolution and reduces the side lobes, and is less sensitive than DMAS to high noise levels at deeper depths. Since the DS-DMAS approach was proposed, it has been adopted in photoacoustic imaging [36–38]. Very recently, Song et al. proposed a modified version of DS-DMAS for ultrasound imaging [39]. In the first phase of DMAS beamforming, they combined pairs of signals with the same spatial lag into a new signal. Then they processed the new signal with F-DMAS beamforming to produce the final output. They showed that combining the autocorrelation signals with the DMAS, the image quality of DS-DMAS is slightly improved as compared with the DS-DMAS.

Several groups have proposed a nonlinear beamformer based on p -th root compression (NL- p -DAS) and applied it to PA and US imaging [40–42]. The results have showed that compared with DAS, and DMAS, the NL- p -DAS ($p > 2$) leads to lower side lobes. However, different than DMAS family of algorithms which is based on autocorrelation approach to improve PA and US signal coherence, the p -th root compression may compress both signal and artifacts depending on the relative strengths of the two parts. The p -th power applied to the coherent beam sum may or may not compensate the signal loss depending on the constructive and destructive interferences. Thus, the optimal choice of p -th root is tricky and highly depends on the imaging medium. Recently, Cho et al. modified the NL- p -DAS technique and performed p -th root operation on the spectral domain data (NL- p -SMS) instead of the temporal domain data, which could reduce the grainy speckles and frequency distortion caused by p -th root in temporal domain data, and dark area artifacts [43]. The algorithm remains to be tested on more clinical data.

The coherence factor (CF) [44] is widely used for aberration correction and side lobe suppression in PA and US imaging. Jeon et al. combined the DMAS algorithm with CF for clinical PA imaging [45]. Mozaffarzadeh et al. combined MV with CF to achieve better resolution in PA imaging [46]. Spadin et al. compared the frequency-domain and delay-and-sum PA image reconstruction with CF weighting [47]. Mukaddim et al. applied spatiotemporal CF to in vivo cardiac PA image beamformation [48]. Bell et al. applied short-lag spatial coherence beamforming to cardiac ultrasound imaging [49].

Here we propose an improved beamformer, named DMAS-LAG-CF which combines lag-based DMAS (DMAS-LAG) [39] with CF to improve spatial resolution and image contrast for better in vivo ovarian cancer diagnosis. To our best knowledge, this is the first time that DMAS-LAG-CF has been implemented and applied to photoacoustic imaging, especially for clinical cancer studies. Due to the nonlinear process of DMAS-LAG-CF, the reconstructed image intensity is not linearly proportional to the initial PA pressure. Therefore, the typical linear unmixing method for calculating the relative total hemoglobin concentration and oxygen saturation is not suitable. However, the proposed DMAS-LAG-CF can achieve better image contrast using a single wavelength in near real-time imaging.

2. Materials and methods

2.1. Proposed reconstruction algorithm

The improved version of DMAS [29] is formulized as

$$s_{ij}(t) = \text{sign}(s_i(t)s_j(t)) \cdot \sqrt{|s_i(t)s_j(t)|} \quad (1)$$

$$y_{DMAS}(t) = \sum_{i=1}^{N-1} \sum_{j=i+1}^N s_{ij}(t), \quad (2)$$

where s_i and s_j are the delayed signals received by the i^{th} and j^{th} elements, respectively. N is the number of elements used to receive signals. y_{DMAS} is the DMAS beamformed output. In this algorithm, due to the multiplication and summation, the central frequency, f_0 , of the original signals is shifted to DC and $2f_0$ in the output. Thus, the output is filtered by a bandpass filter, centered at $2f_0$, to recover frequency components while removing DC components. Equation (2) can be expanded as

$$y_{DMAS} = [\bar{s}_1\bar{s}_2 + \bar{s}_2\bar{s}_3 + \cdots + \bar{s}_{N-2}\bar{s}_{N-1} + \bar{s}_{N-1}\bar{s}_N] + [\bar{s}_1\bar{s}_3 + \bar{s}_2\bar{s}_4 + \cdots + \bar{s}_{N-3}\bar{s}_{N-1} + \bar{s}_{N-2}\bar{s}_N] \\ + \cdots + [\bar{s}_1\bar{s}_{N-1} + \bar{s}_2\bar{s}_N] + [\bar{s}_1\bar{s}_N], \quad (3)$$

where $\bar{s}_i = \text{sign}(s_i)\sqrt{|s_i|}$, for $1 \leq i \leq N$. In this equation, signal pairs with the same lag are grouped in separate brackets [39]. We consider the output of each of these brackets as a new signal and call it ss_i , which is defined as

$$ss_i = \sum_{k=1}^{N-i} \bar{s}_k \cdot \bar{s}_{k+i}, \quad (4)$$

for $1 \leq i \leq N-1$. We combine each ss_i with the CF, and obtain a new parameter, defined as

$$ccs_i = \sum_{k=1}^{N-i} \overline{cs}_k \cdot \overline{cs}_{k+i}, \quad (5)$$

for $1 \leq i \leq N-1$, where $cs_i = \frac{(\sum_{i=1}^N s_i)^2}{N \sum_{i=1}^N (s_i)^2} \cdot s_i$, $\overline{cs}_i = \text{sign}(cs_i)\sqrt{|cs_i|}$. Then the final DMAS-LAG-CF can be formulated as

$$y_{DMAS-LAG-CF} = \sum_{i=1}^{N-2} \sum_{j=i+1}^{N-1} \overline{ccs}_i \cdot \overline{ccs}_j. \quad (6)$$

The schematic diagram of DMAS-LAG-CF is shown in Fig. 1. All the symbols used in the diagram are the same as those in the Eq. (5) and (6). This diagram depicts how to synthesize new

signals in terms of different lags which are discriminated by different colors in Fig. 1. To compare the performance of DMAS-LAG-CF with DMAS-CF, we also implemented the DMAS-CF algorithm which is formulated as

$$y_{DMAS-CF} = \sum_{i=1}^{N-1} \sum_{j=i+1}^N \text{sign}(cs_i \cdot cs_j) \cdot \sqrt{|cs_i cs_j|}. \quad (7)$$

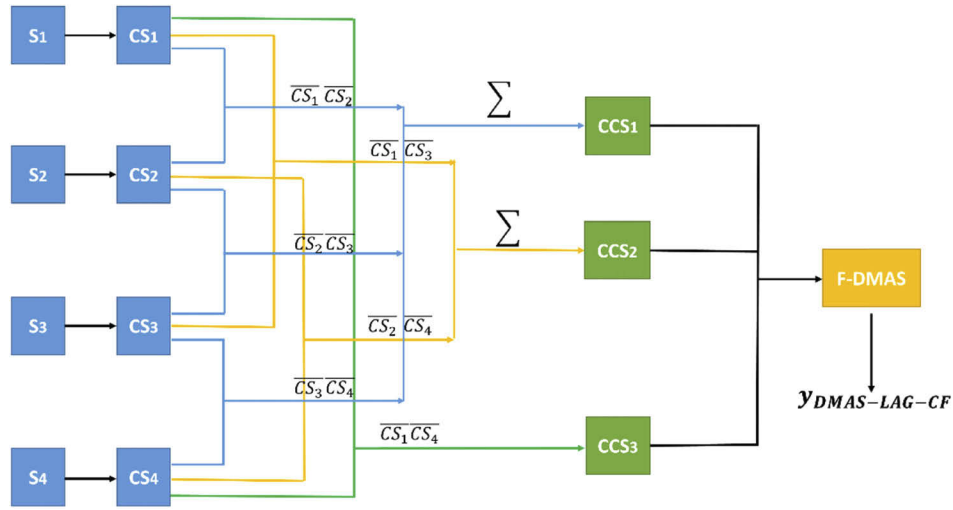


Fig. 1. Schematic diagram of DMAS-LAG-CF.

2.2. Co-registered PAT/US imaging system

Our co-registered PAT/US imaging system, described in detail in [10,50], consists of a Ti:sapphire (Symphotics TII, LS-2122) optically pumped with a Q-switched Nd: YAG laser (Symphotics TII, LS-2134) to deliver pulsed laser light (10–30 ns pulse duration, 15 Hz pulse repetition rate), a commercial ultrasound system (EC-12R, Alpinion Medical Systems), and a 128 channel curved transvaginal ultrasound transducer (central frequency: 6 MHz, 80% bandwidth). For each imaging position, the system is programmed to record data sequentially at wavelengths of 730, 780, 800, and 830 nm. The pulsed laser light output at tissue surface is below the ANSI safety limit [51]. Note that, due to the nonlinear process of DMAS-LAG-CF, we use only a single wavelength (730 nm) for the following data processing.

2.3. Ovarian cancer patients

A total of 28 patients enrolled from May 2017 to November 2018, were evaluated in this study. Among these patients, both ovaries were imaged in 12 patients; for the remaining 16 patients, only one suspicious ovary with pathological evaluation was imaged. Among 40 ovaries, 10 had invasive serous or endometrioid ovarian cancer, one had a serous borderline tumor, and the rest were benign/normal ovaries. The borderline tumor was included in the cancerous group in the analysis. This study protocol was approved by the Institution Review Board of Washington University Medical School in St. Louis and all patients signed the informed consent.

2.4. Feature selection and classification

Histograms of PAT image envelopes were computed from the malignant and benign/normal groups, and three features—variance, skewness, and kurtosis, (see Appendix A)—were extracted

quantitatively from the histograms to characterize these two groups. The mean values of PAT image envelopes (PAT_mean) within the regions of interest (ROIs) and the corresponding histogram features were tested using two-sample two-sided Student's *t* tests. A feature with a *p*-value equal to or less than 0.05 ($p \leq 0.05$) was considered significant.

Next, we performed a regression analysis on our data to find the best logistic regression model. Models were developed for three sets of independent features extracted from all the patients: PAT_mean alone, PAT_mean and kurtosis combined, and PAT_mean and skewness. Skewness and kurtosis were not evaluated as a set because they are highly correlated by Spearman's cross correlation. For each model, the receiver operating characteristic (ROC) curve and the area under the curve (AUC) were calculated, and the best model was determined by the highest AUC value.

2.5. Performance evaluation

First, we compared the spatial resolution and side lobe performance of the DAS, DMAS, DMAS-CF, DMAS-LAG, and DMAS-LAG-CF beamforming algorithms, using a simulated numerical phantom. The raw data consisted of seven equidistant pairs of point targets located at seven different depths. The transducer array geometry used in the simulation was linear, with 64 elements (element pitch, 231 μm ; kerf, 38.5 μm ; element height and width, 14 mm and 192.5 μm ; lambda, 385 μm). The full width at half maximum (FWHM) was calculated from the fitted Gaussian curve after deconvolution with the transfer function of the transducer, and this value is used as a measure of the spatial resolution throughout the paper. We compared the performance of DAS, DMAS, DMAS-CF, DMAS-LAG, and DMAS-LAG-CF by imaging a 200 μm diameter black thread perpendicular to the imaging plane and submerged in a water tank filled with calibrated intralipid solution (Fresenius Kabi, USA) with a reduced scattering coefficient (μ'_s) of 4 cm^{-1} and an absorption coefficient (μ_a) of 0.02 cm^{-1} .

Next, we compared the contrast ratios (CRs) of a simulated contrast phantom as reconstructed by the DAS, DMAS, DMAS-CF, DMAS-LAG, and DMAS-LAG-CF beamforming algorithms. Following the same procedure as in [52,53], we modeled a benign cyst as a 15-mm-diameter sphere within a tissue mimicking medium (the cube size was 84 * 84 * 70 mm) at a depth of 20 mm. The tissue mimicking background medium's μ_a was set as 0.1 cm^{-1} , and μ'_s was set as 5 cm^{-1} . As the positive contrast (higher than the background μ_a), the cyst's μ_a was set as 0.9 cm^{-1} and μ'_s was set as 0.0001 cm^{-1} to mimic an aqueous medium without scattering. The CR index is defined as $\text{CR} = 20 \log_{10} I_{\text{target}} / I_{\text{background}}$, where I_{target} and $I_{\text{background}}$ are the PAT_mean in the target and background areas. The ideal CR based on μ_a ratio is 19dB.

We then applied the DAS, DMAS, DMAS-CF, DMAS-LAG, DMAS-LAG-CF algorithms to ovarian cancer patient data to improve the image contrast between the PAT image envelopes of the cancerous masses and those of the benign/normal lesions. We calculated the PAT_mean in each ROI and extracted the histogram features from the corresponding PAT image envelopes. Ultrasound images were employed to select an ROI corresponding to the lesion. Note that we selected only one normal or cancer area for each ovary. Thus, a total of 11 cancer areas and 29 normal areas were obtained for quantitative feature extraction and classification.

3. Results

As shown in Fig. 2(a), the simulated point target pairs reconstructed by DMAS-LAG-CF are smaller than those reconstructed by the other algorithms. Based on the 1-D profile from DMAS-LAG-CF in Fig. 2(b), the two peaks corresponding to the two point targets are sharpest and the side lobes are lowest. Also, from the lateral resolution calculated at three different depths (49, 59, 69 mm) shown in Fig. 2(c), the lateral resolution for DMAS-LAG-CF is around 1.70, 1.52, 1.10, and 1.20 times better than the values for DAS, DMAS, DMAS-CF, and DMAS-LAG.

In Fig. 3, the black thread cross-section reconstructed by DMAS-LAG-CF is thinnest. Based on 1-D profiles across the black thread, the lateral resolution of DMAS-LAG-CF is respectively

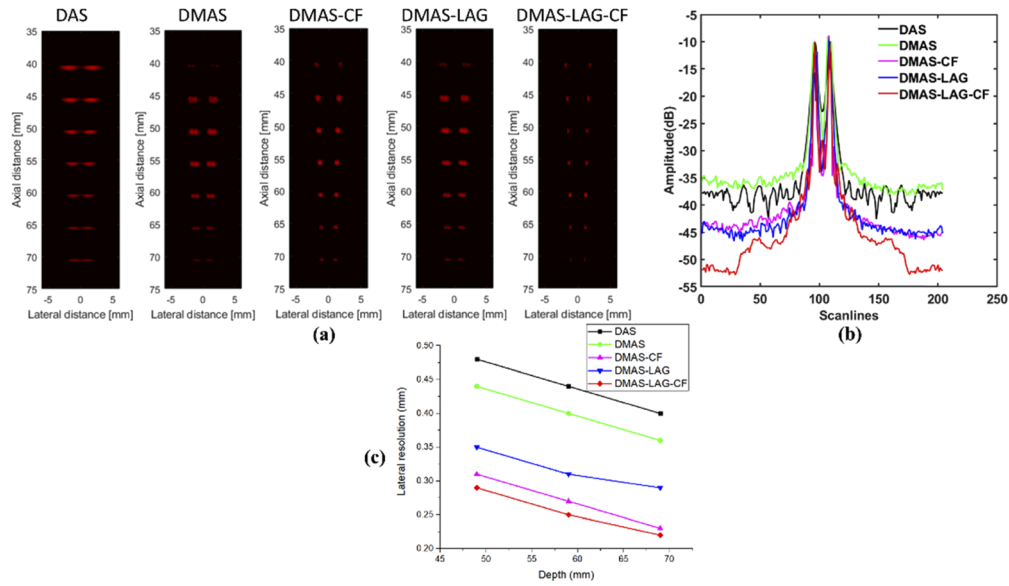


Fig. 2. (a) Simulated point target pairs reconstructed by DAS, DMAS, DMAS-CF, DMAS-LAG, and DMAS-LAG-CF (dynamic range, 15 dB). (b) The corresponding 1-D profiles of the images in (a) at a depth of 49 mm. (c) The lateral resolution performance for DAS, DMAS, DMAS-CF, DMAS-LAG, and DMAS-LAG-CF at depths of 49 mm, 59 mm, and 69 mm.

around 1.39, 1.30, 1.07, and 1.15 times better than those of DAS, DMAS, DMAS-CF, and DMAS-LAG. The theoretical value of the spatial resolution is around 0.20 mm.

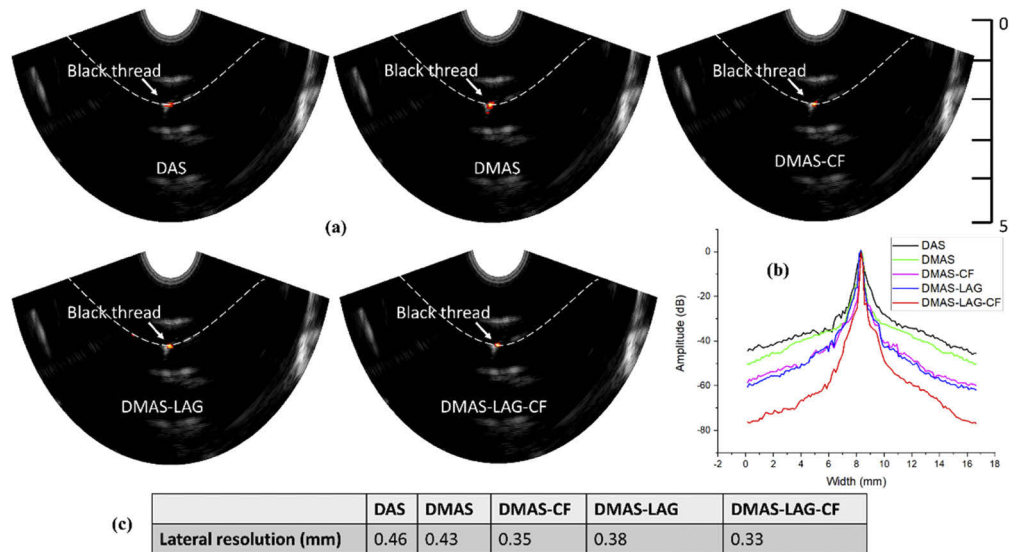


Fig. 3. (a) Black thread images reconstructed by the DAS, DMAS, DMAS-CF, DMAS-LAG, and DMAS-LAG-CF algorithms (dynamic range, 10 dB; scale, cm). (b) The corresponding 1-D profiles across the black thread (averaged from 20 consecutive envelopes along the depth). (c) Calculated spatial resolution results based on the 1-D profiles across the black thread.

The geometry of the simulated contrast phantom is shown in Fig. 4(a). We selected two background areas for fair judgement (the dashed square marked as 2 and 3 in Fig. 4(b), Fig. 4(c), Fig. 4(d), Fig. 4(e), and Fig. 4(f)), with corresponding contrast ratios of CR1 and CR2. Comparing Fig. 4(b), Fig. 4(c), Fig. 4(d), Fig. 4(e), and Fig. 4(f), we can see that the image reconstructed by DMAS-LAG-CF has the best contrast between the target and background area. Quantitatively, the CR1 of DMAS-LAG-CF was around 12.19 dB, 8.81 dB, 7.47 dB, and 4.10 dB higher than those of DAS, DMAS, DMAS-CF, and DMAS-LAG, based on the mean values of the image intensity calculated in the target and background areas. Also the CR2 of DMAS-LAG-CF was around 9.35 dB, 6.83 dB, 5.85 dB, and 2.96 dB higher than those of DAS, DMAS, DMAS-CF, and DMAS-LAG. On average, the CR of DMAS-LAG-CF was around 10.77 dB, 7.82 dB, 6.66 dB, and 3.53 dB higher than those of DAS, DMAS, DMAS-CF, and DMAS-LAG. In Fig. 4(c), Fig. 4(d), Fig. 4(e), and Fig. 4(f), one small dot appears underneath the chosen target area because the scattering coefficient of the cyst target is very low, and a small portion of light propagates through the target area with higher light fluence than background to illuminate the region underneath. Also, one red area appears right on top of the chosen target area close to the transducer face, because the light has traveled only a very short distance and has not yet been fully diffused.

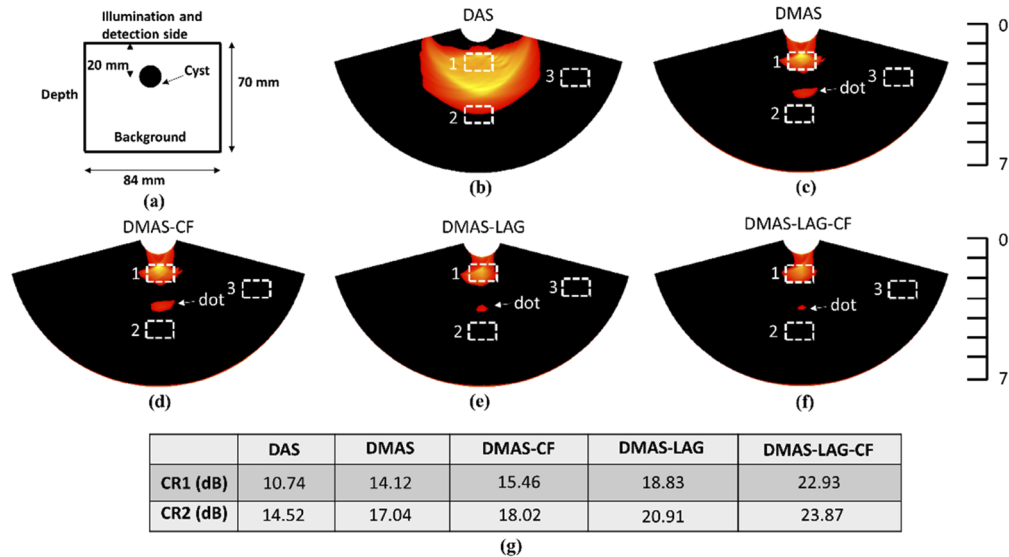


Fig. 4. (a) Phantom geometries used for simulations. Simulated contrast phantom images reconstructed by the DAS (b), DMAS (c), DMAS-CF (d), DMAS-LAG (e), and the DMAS-LAG-CF (f) algorithms (dynamic range, 10 dB; scale bar, cm). (g) Calculated CR results based on the mean values of the image intensity in the target and background areas (target areas: dashed square areas 1 of (b), (c), (d), (e), and (f); background areas: dashed square areas 2 and 3 of (b), (c), (d), (e), and (f)). CR1 and CR2 correspond to the dashed square areas 2 and 3.

Figure 5 shows one example PAT image (730 nm) from an ovarian cancer, calculated by DAS, DMAS, DMAS-CF, DMAS-LAG, and DMAS-LAG-CF. The CRs were computed from the two background regions and the target central region as marked by the white boxes in the images. The average CRs computed from the two background regions were given in the table. For the cancer case, the DMAS-LAG-CF improved CR of DAS, DMAS, DMAS-CF and DMAS-LAG by 6.9 dB, 5.1 dB, 2.5 dB, and 1.2 dB, respectively. For the benign case, the corresponding improvements of CR were 7.6 dB, 4.6 dB, 3.4 dB, 1.5 dB, respectively. Thus, DMAS-LAG-CF performs the best on

improving CR. However, since the clinical significance is the diagnostic accuracy between cancer and benign/normal ovarian lesions, we have evaluated PAT-mean ratios of the two examples. The PAT-mean ratios of the cancer to benign lesions are 2.32, 2.21, 2.16, 2.11, and 2.03 for DMAS-LAG-CF, DMAS-LAG, DMAS-CF, DMAS, and DAS, respectively. DMAS-LAG-CF improves PAT-mean ratio by 5%, 7%, 10%, and 14% compared with DMAS-LAG, DMAS-CF, DMAS, and DAS.

Figure 6 shows boxplots for the PAT_mean and histogram features (kurtosis, skewness), across the entire set of 28 patients between the benign/normal and cancer areas for DAS, DMAS, DMAS-CF, DMAS-LAG, and DMAS-LAG-CF. The variance feature, not shown here, is not significant for all five algorithms. The number n in the plots corresponds to the total number of areas. In terms of three extracted histogram features (PAT-mean, kurtosis, and skewness), the p values between cancers and benign/normal lesions obtained from DMAS-LAG and DMAS-LAG-CF were lower than those of the standard DAS beamforming algorithm.

Figure 7 shows the ROC curves and AUC values of the fitting data sets, using regression models for DAS (Fig. 7(a)), DMAS (Fig. 7(b)), DMAS-CF (Fig. 7(c)), DMAS-LAG (Fig. 7(d)), and DMAS-LAG-CF (Fig. 7(e)). When skewness and PAT_mean are included in the feature set, the best performances (the highest AUC values for the data set) are 0.87, 0.86, 0.82, 0.89, and 0.91 for DAS, DMAS, DMAS-CF, DMAS-LAG, and DMAS-LAG-CF, respectively.

4. Discussion and summary

In this paper, we implemented an improved beamformer, named DMAS-LAG-CF, which combines lag-based delay multiply and sum with coherence factor.

We first compared the spatial resolution and contrast performance of the DAS, DMAS, DMAS-CF, DMAS-LAG, and DMAS-LAG-CF beamforming algorithms using a simulated numerical phantom. Compared to the performances of DAS, DMAS, DMAS-CF, and DMAS-LAG, the lateral resolution for DMAS-LAG-CF was around 1.70, 1.52, 1.10, 1.20 times better.

Then we imaged a 200 μm diameter black thread perpendicular to the imaging plane and submerged in a water tank filled with calibrated intralipid solution and found that the lateral resolution of DMAS-LAG-CF was around 1.39, 1.30, 1.07, 1.15 times better than those of DAS, DMAS, DMAS-CF, and DMAS-LAG. Afterwards, we compared the CR performance of DAS, DMAS, DMAS-CF, and DMAS-LAG, and DMAS-LAG-CF using a simulated contrast phantom.

On average, the CR for DMAS-LAG-CF was around 10.77 dB, 7.82 dB, 6.66 dB, and 3.53 dB higher than those of DAS, DMAS, DMAS-CF, and DMAS-LAG. Thus, the improvement of DMAS-LAG-CF over other algorithms is in image contrast. The two clinical examples have demonstrated similar improvement in computed CRs. The corresponding CRs for the cancer case were 6.9 dB, 5.1 dB, 2.5 dB, and 1.2 dB, and CRs for the benign case were 7.6, 4.6, 3.4, and 1.5 dB.

Since the clinical value of diagnostic accuracy is between cancer and benign/normal lesions, we applied the DMAS-LAG algorithm without and with the coherent factor, to patient data to enhance the contrast between PAT images of cancerous masses and that of benign/normal ovarian lesions. In terms of three extracted histogram features (PAT_mean, kurtosis, and skewness), the p values between cancers and benign/normal lesions were lower than those of the standard DAS beamforming algorithm. The best DMAS-LAG-CF regression model achieved an AUC of 0.91, when PAT_mean and skewness were included in the feature set. This is significant in offering diagnosis to patients using photoacoustic imaging co-registered with ultrasound.

The three PAT features are related to the distribution of absorbers inside the ovaries. For example, a cancerous ovary has large clusters of highly absorbing micro-vessels, and it is expected that its PAT histogram should be more skewed towards higher mean values. DMAS-LAG and DMAS-LAG-CF improve PA signal coherence over DAS, and thus these algorithms enhance the contrast between highly absorbing cancerous tissue and benign/normal lesions. Kurtosis

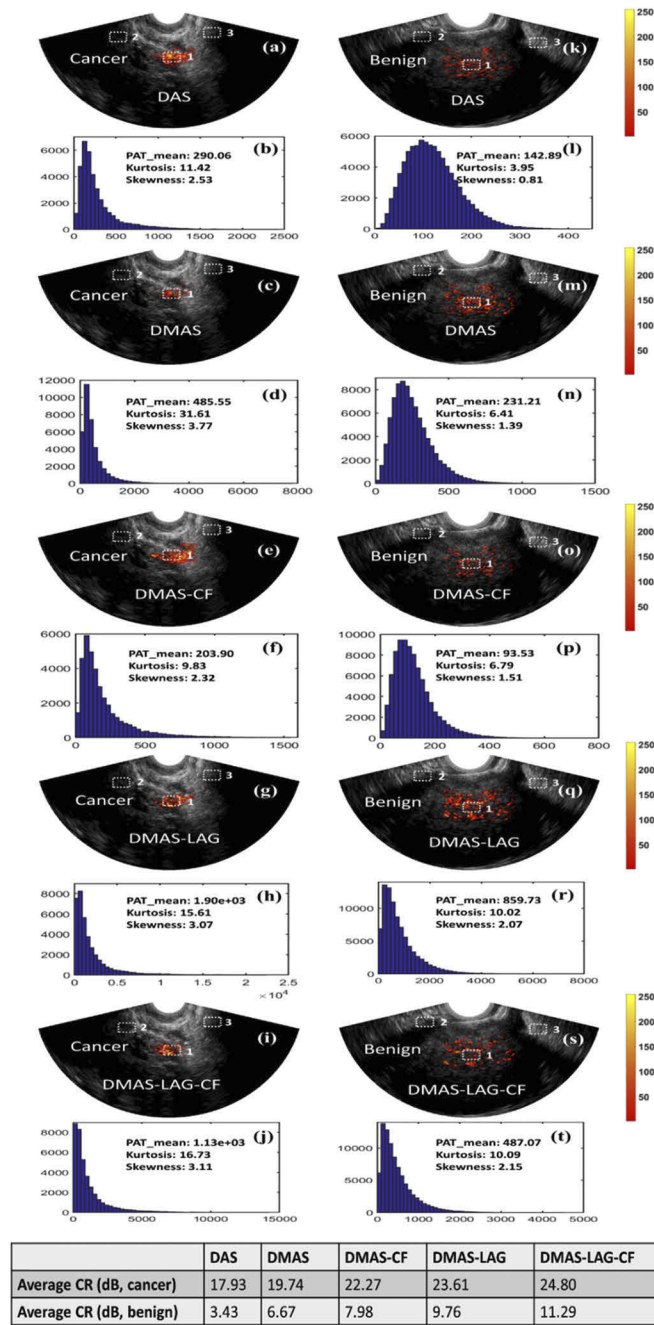


Fig. 5. PAT images (730 nm) and corresponding histogram features extracted from an ovarian cancer (a)-(j) and a benign ovary (k)-(t). All PAT images are displayed with 15dB dynamic range.

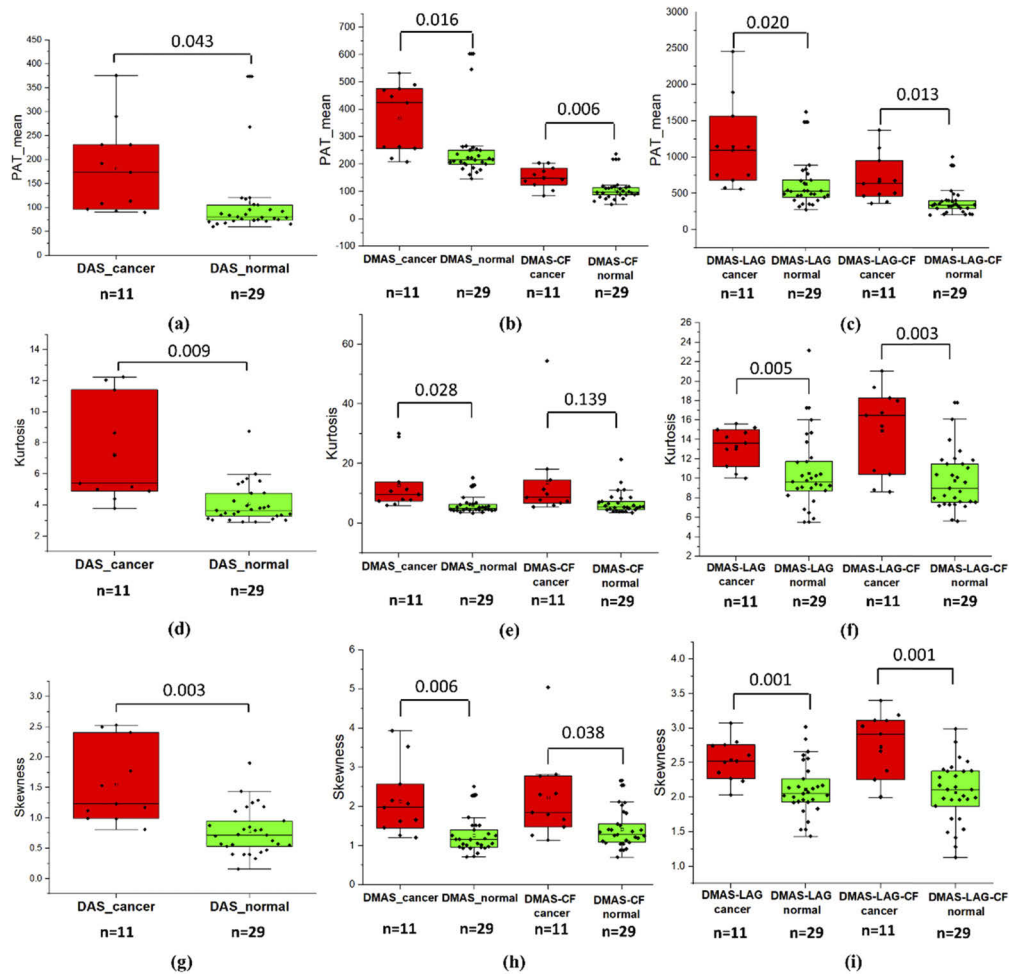


Fig. 6. (a)-(c): Boxplots of mean values of PAT envelopes using (a) DAS, (b) DMAS (left) and DMAS-CF (right), and (c) DMAS-LAG (left) and DMAS-LAG-CF (right). (d)-(f): Boxplots of kurtosis using (d) DAS, (e) DMAS (left) and DMAS-CF (right), and (f) DMAS-LAG (left) and DMAS-LAG-CF (right). (g)-(i): Boxplots of skewness using (g) DAS, (h) DMAS (left) and DMAS-CF (right), and (i) DMAS-LAG (left) and DMAS-LAG-CF (right). The p -value is shown in the associated plot. The number of samples in each group is also shown in the x-axis of each plot.

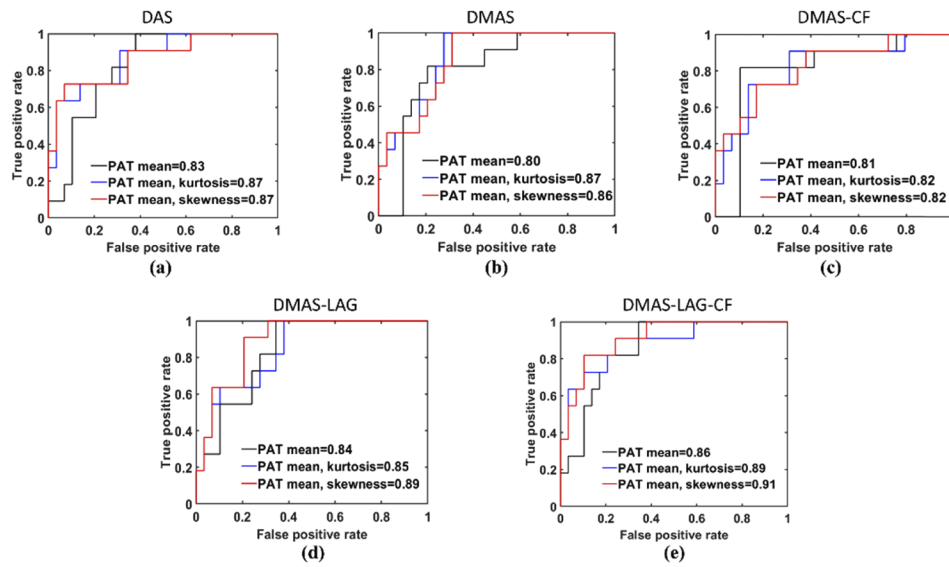


Fig. 7. ROC curves and associated AUC values of five regression models developed to fit the data extracted from all patients. Regression model of DAS (a), DMAS (b), DMAS-CF (c), DMAS-LAG (d), and DMAS-LAG-CF (e).

measures how close the distribution's tail is to the tail of a normal distribution. If there are many outliers in the histogram, the distribution is heavily tailed. Therefore, kurtosis can be a good measure of the number of absorbers that are considered as outliers. Again, DMAS-LAG and DMAS-LAG-CF improve PA signal coherence and therefore increase the deviation of cancerous tissue, with large clusters of highly absorbing micro-vessels, from that of a normal distribution.

DMAS-LAG [39] is essentially the same as the DS-DMAS which improves DMAS by improving off-axis noise levels at deeper depths [35]. Thus, the contrast improvements of DMAS-LAG over DMAS and DMAS-LAG-CF over DMAS-CF are expected. However, both DMAS and DMAS-CF should also improve the diagnostic performance of DAS because they both improve PAT signal coherence by reducing off-axis noise. Only PAT_mean computed from DMAS between cancer and benign/normal groups has a lower p value than that of DAS. We were surprised that the ROC analysis of patient data did not show improvement of DMAS and DMAS-CF over DAS, which warrants further investigation.

Note that, compared with the computational complexity of DAS ($O(N)$, where N is the number of elements), DMAS-LAG-CF has an exponentially higher computational complexity ($O(N^2)$). Also, the bandpass filters involved in the post-processing of the DMAS-LAG-CF rely on two computationally intensive Fourier transforms. In processing a single frame from a patient dataset, the average runtime of our DMAS-LAG-CF algorithm was about 10 times longer than that of DAS. The reconstruction was performed by running MATLAB R2018 on a Windows 10 operating system using an i3-6100 CPU (Intel, Santa Clara, CA, USA) and 16 GB memory. To achieve near real-time clinical application, the processing speed can be improved with a better computational platform and GPU processing. Also, the two-stage signum, absolute, and square root operations slowed down DMAS-LAG-CF. In some application situations, we can perform only one stage of the above operations to improve the processing speed at the expense of slightly lower resolution and higher side lobes. Moreover, we can reduce the lag number for combinational multiplication in the second stage to improve the processing speed at the cost of a decreased effective aperture (spatial resolution).

Overall, this initial study shows that the proposed beamforming algorithm can achieve valuably better image contrast for improved diagnosis of ovarian cancer with a cohort of 28 patients.

DMAS and DMAS-LAG are nonlinear beamformers and the linear unmixing method to compute the relative hemoglobin contrast from multi-wavelength data cannot be implemented directly. This is an inherent limitation of DMAS based beamforming methods. However, the methods can be readily implemented in single wavelength PA imaging for near real time ovarian cancer diagnosis as well as other oncology applications.

Appendix A: Histogram features extraction

The three histogram features can be computed from Eq. (8) to (10), where x_i is the pixel gray level, and N is the total number of pixels.

$$\text{Variance } (\sigma^2) = \frac{1}{N} \sum_{i=1}^N (x_i - \mu)^2 \quad (8)$$

$$\text{Skewness} = \frac{1}{N} \sum_{i=1}^N \left[\frac{x_i - \mu}{\sigma} \right]^3 \quad (9)$$

$$\text{Kurtosis} = \frac{1}{N} \sum_{i=1}^N \left[\frac{x_i - \mu}{\sigma} \right]^4 - 3. \quad (10)$$

Funding. National Cancer Institute (R01CA237664).

Acknowledgements. We sincerely thank Prof. James Ballard for manuscript editing and Lin Chen for valuable help on beamforming implementation.

Disclosures. The authors declare no conflicts of interest.

References

1. L. V. Wang and S. Hu, "Photoacoustic tomography: in vivo imaging from organelles to organs," *Science* **335**(6075), 1458–1462 (2012).
2. L. V. Wang and J. Yao, "A practical guide to photoacoustic tomography in the life sciences," *Nat. Methods* **13**(8), 627–638 (2016).
3. A. A. Oraevsky, B. Clingman, J. Zalev, A. T. Stavros, W. T. Yang, and J. R. Parikh, "Clinical optoacoustic imaging combined with ultrasound for coregistered functional and anatomical mapping of breast tumors," *Photoacoustics* **12**, 30–45 (2018).
4. L. Lin, P. Hu, J. Shi, C. M. Appleton, K. Maslov, L. Li, and L. V. Wang, "Single-breath-hold photoacoustic computed tomography of the breast," *Nat. Commun.* **9**(1), 1–9 (2018).
5. W. Roll, N. A. Markwardt, M. Masthoff, A. Helfen, J. Claussen, M. Eisenblätter, and V. Ntziachristos, "Multispectral optoacoustic tomography of benign and malignant thyroid disorders: a pilot study," *J. Nucl. Med.* **60**(10), 1461–1466 (2019).
6. M. Yang, L. Zhao, X. He, N. Su, C. Zhao, H. Tang, and B. Zhang, "Photoacoustic/ultrasound dual imaging of human thyroid cancers: an initial clinical study," *Biomed. Opt. Express* **8**(7), 3449–3457 (2017).
7. K. Peng, L. He, B. Wang, and J. Xiao, "Detection of cervical cancer based on photoacoustic imaging—the in-vitro results," *Biomed. Opt. Express* **6**(1), 135–143 (2015).
8. G. Yang, E. Amidi, W. C. Chapman, S. Nandy, A. Mostafa, H. Abdelal, and Q. Zhu, "Co-registered photoacoustic and ultrasound imaging of human colorectal cancer," *J. Biomed. Opt.* **24**(12), 1–13 (2019).
9. X. Leng, W. Chapman, B. Rao, S. Nandy, R. Chen, R. Rais, and Q. Zhu, "Feasibility of co-registered ultrasound and acoustic-resolution photoacoustic imaging of human colorectal cancer," *Biomed. Opt. Express* **9**(11), 5159–5172 (2018).
10. S. Nandy, A. Mostafa, I. S. Hagemann, M. A. Powell, E. Amidi, K. Robinson, and Q. Zhu, "Evaluation of ovarian cancer: initial application of coregistered photoacoustic tomography and US," *Radiology* **289**(3), 740–747 (2018).
11. E. Amidi, A. Mostafa, S. Nandy, G. Yang, W. Middleton, C. Siegel, and Q. Zhu, "Classification of human ovarian cancer using functional, spectral, and imaging features obtained from in vivo photoacoustic imaging," *Biomed. Opt. Express* **10**(5), 2303–2317 (2019).
12. C. Liu, M. Xing, B. Cong, C. Qiu, D. He, C. Wang, and T. Ma, "In vivo transrectal imaging of canine prostate with a sensitive and compact handheld transrectal array photoacoustic probe for early diagnosis of prostate cancer," *Biomed. Opt. Express* **10**(4), 1707–1717 (2019).

13. V. S. Dogra, B. K. Chinni, K. S. Valluru, J. V. Joseph, A. Ghazi, J. L. Yao, and N. A. Rao, "Multispectral photoacoustic imaging of prostate cancer: preliminary ex-vivo results," *J. Clinical Imaging Sci.* **3**, 4141 (2013).
14. Y. Wang, Y. Zhan, L. M. Harris, S. Khan, and J. Xia, "A portable three-dimensional photoacoustic tomography system for imaging of chronic foot ulcers," *Quant. Imaging Med. Surg.* **9**(5), 799 (2019).
15. J. Jo, G. Xu, M. Cao, A. Marquardt, S. Francis, G. Gandikota, and X. Wang, "A functional study of human inflammatory arthritis using photoacoustic imaging," *Sci. Rep.* **7**(1), 1–9 (2017).
16. P. J. van den Berg, K. Daoudi, H. J. B. Moens, and W. Steenbergen, "Feasibility of photoacoustic/ultrasound imaging of synovitis in finger joints using a point-of-care system," *Photoacoustics* **8**, 8–14 (2017).
17. J. Jo, C. Tian, G. Xu, J. Sarazin, E. Schiopu, G. Gandikota, and X. Wang, "Photoacoustic tomography for human musculoskeletal imaging and inflammatory arthritis detection," *Photoacoustics* **12**, 82–89 (2018).
18. J. Aguirre, M. Schwarz, N. Garzorz, M. Omar, A. Buehler, K. Eyerich, and V. Ntziachristos, "Precision assessment of label-free psoriasis biomarkers with ultra-broadband optoacoustic mesoscopy," *Nat. Biomed. Eng.* **1**(5), 0068 (2017).
19. J. Kim, Y. H. Kim, B. Park, H. M. Seo, C. H. Bang, G. S. Park, and C. Kim, "Multispectral ex vivo photoacoustic imaging of cutaneous melanoma for better selection of the excision margin," *Br. J. Dermatol.* **179**(3), 780–782 (2018).
20. A. B. E. Attia, S. Y. Chuah, D. Razansky, C. J. H. Ho, P. Malempati, U. S. Dinis, and M. W. P. Tan, "Noninvasive real-time characterization of non-melanoma skin cancers with handheld optoacoustic probes," *Photoacoustics* **7**, 20–26 (2017).
21. American Cancer Society. Cancer facts and figures, 2019, American Cancer Society, Atlanta, GA (2019).
22. D. L. Clarke-Pearson, "Screening for ovarian cancer," *N. Engl. J. Med.* **361**(2), 170–177 (2009).
23. N. J. Finkler, B. E. R. Y. L. Benacerraf, P. T. Lavin, C. A. R. O. L. Wojciechowski, and R. C. Knapp, "Comparison of serum CA 125, clinical impression, and ultrasound in the preoperative evaluation of ovarian masses," *Obstet. Gynecol.* **72**(4), 659–664 (1988).
24. I. Jacobs, D. Oram, J. Fairbanks, J. Turner, C. Frost, and J. G. Grudzinskas, "A risk of malignancy index incorporating CA 125, ultrasound and menopausal status for the accurate preoperative diagnosis of ovarian cancer," *BJOG: An Intl. J. Obstet. & Gynaecol.* **97**(10), 922–929 (1990).
25. B. Van Calster, D. Timmerman, T. Bourne, A. C. Testa, C. Van Holsbeke, E. Domali, and L. Valentin, "Discrimination between benign and malignant adnexal masses by specialist ultrasound examination versus serum CA-125," *JNCI: J. National Cancer Inst.* **99**(22), 1706–1714 (2007).
26. V. Nossov, M. Amneus, F. Su, J. Lang, J. M. T. Janco, S. T. Reddy, and R. Farias-Eisner, "The early detection of ovarian cancer: from traditional methods to proteomics. Can we really do better than serum CA-125?" *Am. J. Obstet. Gynecol.* **199**(3), 215–223 (2008).
27. C. H. E. N. Di-Xia, P. E. Schwartz, L. Xinguo, and Y. Zhan, "Evaluation of CA 125 levels in differentiating malignant from benign tumors in patients with pelvic masses," *Obstet. Gynecol.* **72**(1), 23–27 (1988).
28. H. B. Lim, N. T. T. Nhung, E. P. Li, and N. D. Thang, "Confocal microwave imaging for breast cancer detection: Delay-multiply-and-sum image reconstruction algorithm," *IEEE Trans. Biomed. Eng.* **55**(6), 1697–1704 (2008).
29. G. Matrone, A. S. Savoia, G. Caliano, and G. Magenes, "The delay multiply and sum beamforming algorithm in ultrasound B-mode medical imaging," *IEEE Trans. Med. Imaging* **34**(4), 940–949 (2015).
30. J. Park, S. Jeon, J. Meng, L. Song, J. S. Lee, and C. Kim, "Delay-multiply-and-sum-based synthetic aperture focusing in photoacoustic microscopy," *J. Biomed. Opt.* **21**(3), 036010 (2016).
31. A. Alshaya, S. Harput, A. M. Moubark, D. M. Cowell, J. McLaughlan, and S. Freear, "Spatial resolution and contrast enhancement in photoacoustic imaging with filter delay multiply and sum beamforming technique," In *IEEE International Ultrasonics Symposium (IUS)* (pp. 1–4), (2016).
32. G. Matrone, A. Ramalli, A. S. Savoia, P. Tortoli, and G. Magenes, "High frame-rate, high resolution ultrasound imaging with multi-line transmission and filtered-delay multiply and sum beamforming," *IEEE Trans. Med. Imaging* **36**(2), 478–486 (2017).
33. M. Mozaffarzadeh, A. Mahloojifar, M. Orooji, K. Kratkiewicz, S. Adabi, and M. Nasirivanaki, "Linear-array photoacoustic imaging using minimum variance-based delay multiply and sum adaptive beamforming algorithm," *J. Biomed. Opt.* **23**(2), 1–15 (2018).
34. J. Capon, "High-resolution frequency-wavenumber spectrum analysis," *Proc. IEEE* **57**(8), 1408–1418 (1969).
35. M. Mozaffarzadeh, A. Mahloojifar, M. Orooji, S. Adabi, and M. Nasirivanaki, "Double-stage delay multiply and sum beamforming algorithm: Application to linear-array photoacoustic imaging," *IEEE Trans. Biomed. Eng.* **65**(1), 31–42 (2018).
36. M. Mozaffarzadeh, A. Hariri, C. Moore, and J. V. Jokerst, "The double-stage delay-multiply-and-sum image reconstruction method improves imaging quality in a led-based photoacoustic array scanner," *Photoacoustics* **12**, 22–29 (2018).
37. S. R. Miri Rostami, M. Mozaffarzadeh, M. Ghaffari-Miab, A. Hariri, and J. Jokerst, "GPU-accelerated double-stage delay-multiply-and-sum algorithm for fast photoacoustic tomography using LED excitation and linear arrays," *Ultrasonic Imaging* **41**(5), 301–316 (2019).
38. M. Mozaffarzadeh, M. H. Varnosfaderani, A. Sharma, M. Pramanik, N. de Jong, and M. D. Verweij, "Enhanced contrast acoustic-resolution photoacoustic microscopy using double-stage delay-multiply-and-sum beamformer for vasculature imaging," *J. Biophotonics* **12**(11), e201900133 (2019).
39. K. Song, P. Liu, and D. C. Liu, "Combining autocorrelation signals with delay multiply and sum beamforming algorithm for ultrasound imaging," *Med. Biol. Eng. Comput.* **57**(12), 2717–2729 (2019).

40. M. Polichetti, F. Varray, J. C. Bera, C. Cachard, and B. Nicolas, "A nonlinear beamformer based on p-th root compression-application to plane wave ultrasound imaging," *Appl. Sci.* **8**(4), 599 (2018).
41. M. Mozaffarzadeh, V. Periyasamy, M. Pramanik, and B. Makkiabadi, "Efficient nonlinear beamformer based on Pth root of detected signals for linear-array photoacoustic tomography: application to sentinel lymph node imaging," *J. Biomed. Opt.* **23**(12), 121604 (2018).
42. M. Polichetti, F. Varray, G. Matrone, A. S. Savoia, J. C. Bera, C. Cachard, and B. Nicolas, "A computationally efficient nonlinear beamformer based on p-th root signal compression for enhanced ultrasound b-mode imaging," *In 2017 IEEE IUS*, 1–4, (2017).
43. S. Cho, S. Jeon, W. Choi, R. Managuli, and C. Kim, "Nonlinear pth root spectral magnitude scaling beamforming for clinical photoacoustic and ultrasound imaging," *Opt. Lett.* **45**(16), 4575–4578 (2020).
44. R. Mallart and M. Fink, "Adaptive focusing in scattering media through sound-speed inhomogeneities: The van Cittert Zernike approach and focusing criterion," *J. Acoust. Soc. Am.* **96**(6), 3721–3732 (1994).
45. S. Jeon, E. Y. Park, W. Choi, R. Managuli, K. Jong Lee, and C. Kim, "Real-time delay-multiply-and-sum beamforming with coherence factor for in vivo clinical photoacoustic imaging of humans," *Photoacoustics* **15**, 100136 (2019).
46. M. Mozaffarzadeh, B. Makkiabadi, M. Basij, and M. Mehrmohammadi, "Image improvement in linear-array photoacoustic imaging using high resolution coherence factor weighting technique," *BMC Biomed. Eng.* **1**(1), 10 (2019).
47. F. Spadin, M. Jaeger, R. Nuster, P. Subochev, and M. Frenz, "Quantitative comparison of frequency-domain and delay-and-sum optoacoustic image reconstruction including the effect of coherence factor weighting," *Photoacoustics* **17**, 100149 (2020).
48. R. Al Mukaddim and T. Varghese, "Spatiotemporal coherence weighting for in vivo cardiac photoacoustic image beamformation," *IEEE Trans. Ultrason., Ferroelect., Freq. Contr.* **68**(3), 586–598 (2021).
49. M. A. L. Bell, R. Goswami, J. A. Kisslo, J. J. Dahl, and G. E. Trahey, "Short-lag spatial coherence imaging of cardiac ultrasound data: Initial clinical results," *Ultrasound in Med. & Biol.* **39**(10), 1861–1874 (2013).
50. G. Yang, E. Amidi, S. Nandy, A. Mostafa, and Q. Zhu, "Optimized light delivery probe using ball lenses for co-registered photoacoustic and ultrasound endo-cavity subsurface imaging," *Photoacoustics* **13**, 66–75 (2019).
51. E. Newcomer, G. Yang, B. Sun, H. Luo, D. Shen, S. Achilefu, and Q. Zhu, "Photoacoustic laser effects in live mouse blastocysts: pilot safety studies of DNA damage from photoacoustic imaging doses," *F&S Sci.* **1**(1), 53–58 (2020).
52. N. Akhlaghi, T. J. Pfefer, K. A. Wear, B. S. Garra, and W. C. Vogt, "Multidomain computational modeling of photoacoustic imaging: verification, validation, and image quality prediction," *J. Biomed. Opt.* **24**(12), 1 (2019).
53. M. Heijblom, D. Piras, E. Maartens, E. J. Huisman, F. M. van den Engh, J. M. Klaase, and S. Manohar, "Appearance of breast cysts in planar geometry photoacoustic mammography using 1064-nm excitation," *J. Biomed. Opt.* **18**(12), 126009 (2013).